

Dynamic process of free space excitation of asymmetry resonant microcavity

Fang-Jie Shu,^{1,*} Chang-Ling Zou,² and Fang-Wen Sun^{2,†}

¹*Department of Physics, Shangqiu Normal University, Shangqiu, He'nan 476000, P. R. China.*

²*Key Laboratory of Quantum Information, University of Science and Technology of China, Hefei, Anhui 230026, P. R. China*
(Dated: June 20, 2021)

The underlying physics and detailed dynamical processes of the free space beam excitation to the asymmetry resonant microcavity are studied numerically. Taking the well-studied quadrupole deformed microcavity as an example, we use a Gaussian beam to excite the high-Q mode. The simulation provides a powerful platform to study the underlying physics. The transmission spectrum and intracavity energy can be obtained directly. Irregular transmission spectrum was observed, showing asymmetric Fano-type lineshapes which could be attributed to interference between the different light paths. Then excitation efficiencies about the aim distance of the incident Gaussian beam and the rotation angle of the cavity were studied, showing great consistence with the reversal of emission efficiencies. By projecting the position dependent excitation efficiency to the phase space, the correspondence between the excitation and emission was demonstrated. In addition, we compared the Husimi distributions of the excitation processes and provided more direct evidences of the dynamical tunneling process in the excitation process.

I. INTRODUCTION

Optical microcavity has drawn many attentions owe to its high intracavity field intensity [1]. Light-matter interactions, such as laser [2], nonlinear optics [3], cavity quantum electrodynamics [4, 5], sensors [6] and optomechanics [7], can benefit from the microcavities. No matter these applications are based on active or passive microcavities, energy exchange with the outside is essential. Various shaped asymmetry resonant microcavities (ARCs) (quadrupole [8, 9], spiral [10], stadium [11], Limacon [12], and half-quadrupole-half-circle [13, 14]) were extensively studied recently since light can be collected more efficiently and conveniently through free space in those cavities than in symmetry circular or spherical cavity.

However, most studies put emphasis on the directional emission for efficient collection [5, 9–15], but the inverse processes, i.e. the free space excitation [7], have not been fully explored. An's group performed quadruple droplet pumping experiments, then put mode-coupling theory and numerical simulation forward to explain the experimental phenomenon [16–18]. Their studies focused on the laser emission in a full-chaotic cavity by a plane wave excitation, and the process of chaotic transport in the pumping process was studied indirectly from the laser threshold. However, threshold also depends on the overlap between the pumping mode and lasering mode, and there is also mode competition in the multimode cavity. The laser threshold may not linearly depend on the excitation efficiency of pumping mode. Therefore, the direct evidence of the efficient pump to a passive high-Q modes, and the studies of underlying principle are required. In addition, more perspectives of the free space coupling,

such as the focused beam pump and the spectrum, are lacking.

In this paper, the free space excitation of an ARC by a focused Gaussian beam is studied numerically by boundary elements method (BEM). Then the field distribution, mean intracavity intensity (MII) and the transmission spectrum varying with frequency of the incident beam are also studied. Fano-type lineshape of spectrum is investigated from interference point of view. Excitation efficiency represented by MII is studied by adjusting relative position of the incident beam and the cavity. A comparison between excitation and emission is performed with the help of ray optics. Finally, resorting the Husimi projection of the wave field and the projection of the MII distribution, we discuss the physics mechanism of the free space excitation in several cavities with different degree of deformations.

II. THE BASIC DYNAMICS OF QUADRUPOLE SHAPED MICROCAVITY

Here, we focus on the two dimensional (2D) quadrupole microcavity, which has been studied extensively in theory and experiments [19]. Basic features and underlying physics found in this specific cavity can also extend to other ARCs, like the half-quadrupole-half-circle microcavity. The boundary of quadrupole microcavity in polar coordinate is described by $r(\phi) = R(1 + \varepsilon \cos 2\phi)$ with radius R and degree of deformation ε [8]. In the deformed cavity, the ray dynamics shows quasi-periodic, periodic and chaotic trajectories, corresponding to the regular KAM torus, islands, and chaotic sea in the phase space presentation. Fig. 1(c) (black dots) shows the ray dynamics in quadrupole cavity with deformation $\varepsilon = 0.1$ as an example. Energy of a high quality factor mode is always stored in the vicinity of the regular structure above the critical line by total internal reflection [Fig. 1(a)], part of energy tunnels to the nearby chaotic zone and

* shufangjie@gmail.com

† fwsun@ustc.edu.cn

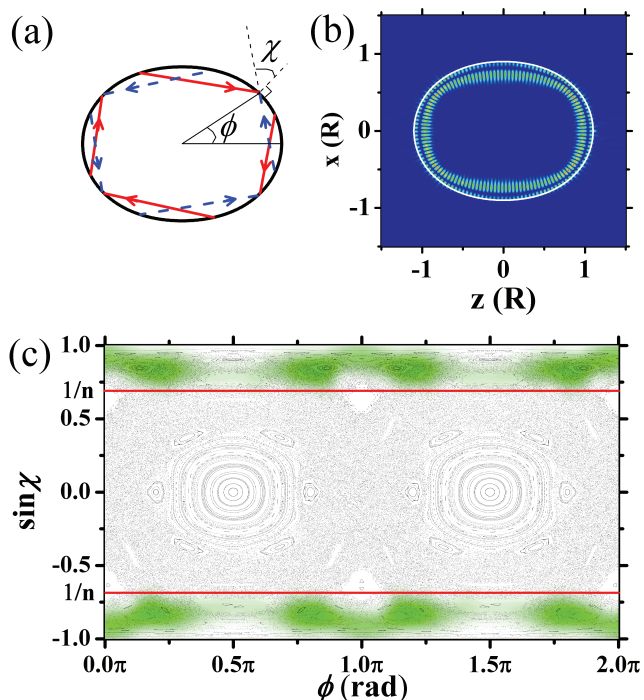


Figure 1. (a) Period-4 rectangle orbits. The ray trajectories are calculated from the location of maximal points in the Husimi projection in (c). Considering the Goos-Hänchen shift, clockwise (red solid line) and counter clockwise (blue dash line) orbits split with each other, and the orbits are not closed. (b) Near field intensity of the order-2 mode. (c) Poincaré Surface of Section (SOS) of the quadrupole cavity (black dots) and Husimi projection (green areas) of the WGM illustrated in (b). In the SOS, ray is recorded as a point with coordinate $(\phi, \sin\chi)$, where ϕ is the polar angle of incident point, and χ is incident angle on the boundary, respectively. The whole SOS of a quadrupole cavity is mixed with Kolmogorov-Arnold-Moser (KAM) torus (curves near the upper and lower boundary of SOS), islands (close curves), and chaotic sea (collection of other dispersed points) structure.

finally leaking out the cavity by reflections. The reflections condense in a few trails, which are called manifold, in phase space [Fig. 5(a)] [20]. The asymmetrical nature of the manifold results in the directional emission.

Ray model just gives basic physics insights of the ARCs. For more underlying physics and precise details, we should also consider the aspect of wave nature of light. The wave functions of high-Q WGMs are calculated numerically (solving Maxwell function using boundary elements method (BEM) [21]). Setting uniform cavity refractive index $n = 1.45$, we search the resonances with quick root searching method [22] at $kR \sim 50$, where kR is also the dimensionless cavity size scale to beam wavelength. Figure 1(b) is a eigenmode of quadrupole cavity near $kR = 50$, it is known as the order-2 mode for existing two intensity peaks along the radial direction. We can see the ray-wave correspondence by Husimi projection of the wave function in phase space, as is shown by the green contour in Fig. 1(c). Eight obviously condensed

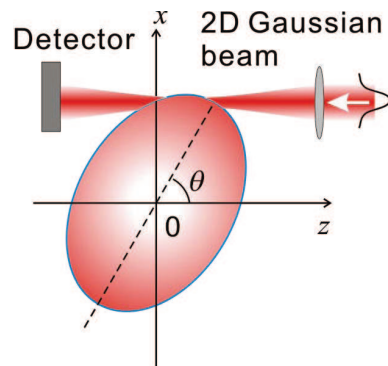


Figure 2. A schematic diagram of an incidence beam, a cavity, and a detector used in the simulation. Note that this configuration is conjugated with former experiments as aim distance $x = -x_{exp}$ and rotation angle $\theta = \frac{\pi}{2} - \theta_{exp}$ [17].

regions are clockwise and counter-clockwise period-4 islands, which corresponds to the period-4 orbits in Fig. 1(a). Noting that the orbits shows a displacement at each reflection, which is attributed to the Goos-Hänchen shift [23]. In the following studies, we focus on this mode to study free space excitation.

III. THE CONFIGURATION OF GAUSSIAN BEAM EXCITATION

Now, we turn to study the free space coupling to the WGM [Fig. 1(b)] by Gaussian beams [Fig. 2]. From the perspective of wave optics, incident focused 2D Gaussian beam reads [24]

$$A(x, z) = \frac{1}{\sqrt{1-i\zeta}} \exp\left[-\frac{(x-x_0)^2}{\omega_0^2(1-i\zeta)} - ikz\right]. \quad (1)$$

Here $\zeta = 2z/b$ is the dimensionless longitudinal location defined in terms of the confocal length $b = k\omega_0^2$, and ω_0 is the beam waist. This Gaussian beam is set as $\omega_0 = 0.3R$, and focus on $z = 0$ line. The relatively narrow waist of the Gaussian beam can be obtained in an experiment by a convergent lens, and benefit the coupling efficiency.

The coupling efficiency depends on the excitation condition of the Gaussian beam, i.e. the direction of the beam and the excitation point on the cavity boundary. So, we rotate the cavity around the original point, and shift the incident beam parallel along x axis. Thus, the coupling config can be represented by two parameters (θ, x) , where θ is angle from axis z to major axis of the quadrupole, and x is the aiming distant between the axial line of the Gaussian beam and the central point of the cavity, which is just the numerical value of x coordinate of the axial line in our coordinates system.

In the first place, an on-resonance and an off-resonance excited patterns of light intensity in cavity with $\varepsilon = 0.1$ are shown in Figs. 3(a) and 3(b). All wave simulations are performed by BEM, which solves the Helmholtz equa-

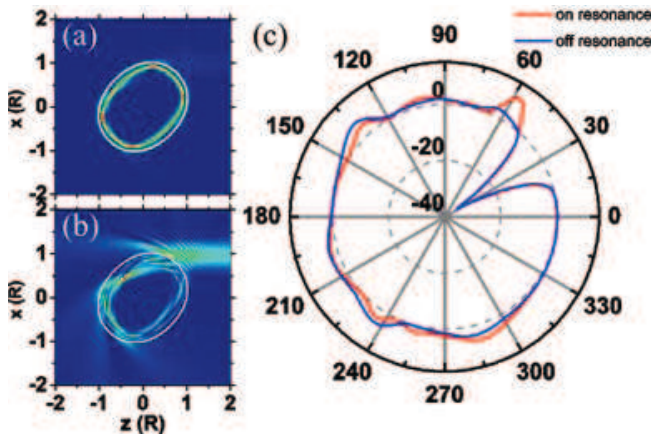


Figure 3. False color intensity patterns of excited cavity using on-resonance (a) and off-resonance (b) incident beam. White lines are the boundaries of the cavity. (c) Angular distributions of outward energy flow through a circle with radius $1.8R$ correspond to the pattern (a) (red line) and (b) (blue line), respectively. A positive value indicates the outflow, a negative value indicates inflow. Parameters: $kR = 49.726$ (on), 49.9 (off), $\phi = 45^\circ$, $x = 0.97$, $\varepsilon = 0.1$.

tion of the electromagnetic field with particular boundary conditions. For simplicity but without loss of generality, only transverse magnetic mode is taken into account. In this polarization, electric field vector is vertical to the cavity plane. The field amplitude and its derivative are both continuous on the interfaces of dielectrics. Incident beam frequency $kR = 49.726$ (49.9) is chosen for on-resonant (off-resonant) coupling, $\theta = 45^\circ$, and $x = 0.97$ are set for getting high intracavity intensity. As is shown in Fig. 3, normalized 2D Gaussian incident beam is partly coupled into the cavity.

In the on-resonance case, notable intensity lies near the cavity boundary forming the whispering gallery like mode, which is consistent with a traveling wave mode corresponding to the order-2 resonance mode at the same kR [Fig. 1(b)]. There is no interference fringe along the ϕ in Fig. 3(a), which is due to only counter-clockwise traveling WGM excited in such excitation configure with a focus Gaussian beam pumping away from the center of the cavity. When it comes to off-resonance case, the cavity field is very different from the eigenmode field. The incidence beam will be refracted into the cavity, reflect along the cavity boundary several times, and finally leak out by refraction [25]. Due to the chaotic ray dynamics, the rays show large expansion in the r direction. This large expansion can also be interpreted as excitation of multiple low-Q modes. The field of which shows higher radial quantum number. These multiple interference also occurs in the on-resonance case, but is not visible due to high resonant field intensity. Note that the incident Gaussian beam is also not visible in the on-resonance condition, which is due to the greatly enhanced cavity field making the relatively low intensity of pumping field invisible. In order to evaluate the intensity in the cavity,

we introduce the MII as average intensity index. When the maximum intensity of the incident Gaussian beam on the waist line is set to a unit as reference intensity, the MII is proportional to coupling efficiency and the Q of a mode. For a particular mode, such as order-2 mode that we concerned, Q is fixed, so the MII represents the coupling efficiency directly. The MIIs are 5.02 and 0.23 for on-resonance and off-resonance excitation, respectively. MII of on-resonance excitation is much larger than that of off-resonance excitation. So in the figure of relative intensity pattern [Fig. 3(a)] Gaussian beam leaves only a dim trace against to the strong intracavity intensity.

Moreover, angular distributions of radial energy flows of on-resonance and off-resonance [Fig. 3(c)] were calculated by the Poynting vector in radial direction $\vec{p} \cdot \vec{n} = \text{Im}(E^* \cdot \partial_v E) / 2\omega\mu$ [26] on a circle with radius of $1.8R$ and center on the original point, where $\partial_v = \vec{v} \cdot \nabla$ is the normal derivative on radial direction \vec{n} , ω is angular frequency, and μ is relative permeability. The flow is negative at 30 degree, which shows the position of the incident Gaussian beam, while the other region is always positive which indicates the outgoing field. For both on- and off- resonance, the net flow as the sum of energy flow in all direction is zero, which indicates that the energy conservation is preserved, i.e. the ideal passive cavity (with real refractive index) does not produce or consume energy. It can be seen from the Fig. 3(b) that the energy flow distribution of off-resonance excitation mainly embodies the redistribution of the incident energy by cavity-caused scattering. In the on-resonance case, there is also the emission from resonant modes. So, two emission peaks of the order-2 CCW mode emerge near 60° and 240° on detector circle in Fig. 4(c), respectively. The interference between the emission of high-Q mode and reflection light of multiple beam also give rise to the modulation of distribution of energy flow in other directions.

IV. THE TRANSMISSION SPECTRUM

Similar with experiment, through a frequency scan to the incident beam, we can obtain the spectrum by using a detector with fixed relative positions of incident Gaussian beam and microcavity [with $\theta = 45^\circ$ and $x = 0.97$]. The energy [Fig. 4 red curves] is the integration of the outward energy flow through the line detector. In addition, the MII spectrum was also recorded [Fig. 4 blue curve]. The transmission spectrum near $kR = 50$ shows the shape of the periodic low-frequency harmonized wave superimposed with high-frequency spikes. Therein, the low-frequency harmonized modulation is interference of light that undergo different quasi-period rounds [25]. The modulation period is about $0.7 \sim 1/n$, i.e. roughly corresponding to an optical distance of one round trip.

On the periodically modulated spectra background, there are many sharp symmetry dips, peaks and asymmetric Fano-type line shapes in the transmission spec-

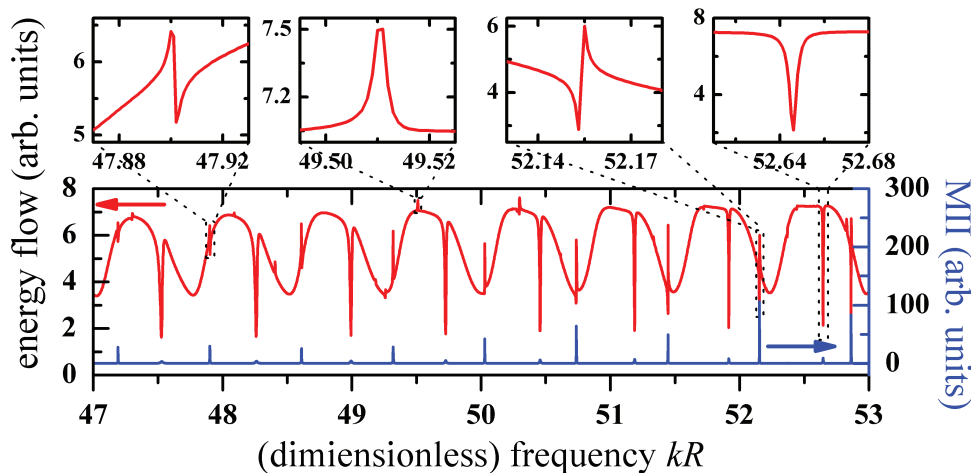


Figure 4. (color online) Spectrum of energy flow (red curves) and mean intracavity intensity (blue curves). The enlarged scales are four typical lineshapes in transmission spectrum.

trum. Comparing with the MII spectra, these sharp variations correspond to a magnified spikes in MII. The correspondence indicates that the formation of those line shapes is related to the on-resonance excitation. We note that the MII spectrum clearly shows two sets of resonance peaks. The set with larger intervals of adjacent lines and larger MII is order-1 modes and the other is order-2 modes which are concerned in this paper. Different from the Lorentz line shape in the transmission spectrum of waveguide coupled cavity, here the line shapes are formed by the interference between emission light of resonance CCW mode and the scattered light by multiple beam interference.

There are two different paths for light to transmit from source to detector: (1) the light coupling to the high-Q cavity mode and emitted from the mode, i.e. direct scattering from high-Q mode (2) the light transmitted after multiple beam interference, or we can say scattering from multiple low-Q modes. The final collected energy is given by

$$E(\delta) = E_{mul}e^{i\alpha} - E_{res}e^{i\beta} \frac{1}{i\delta/\kappa + 1}. \quad (2)$$

Here, δ is the frequency detuning, κ is the linewidth of high-Q mode, α and β are phase factors that denotes the phase variance between source and detector, E_{mul} and E_{res} are the amplitude (real number) of the multiple beam interference and resonance scattered light. For the multiple beam interference, the low-Q modes involved have linewidth much larger than κ , thus the phase α is almost constant for $\delta/\kappa \sim 1$. From the formula, the phase difference $\Delta = \alpha - \beta$ determines collected transmission spectra. (i) $\Delta = 0$ gives symmetry Lorentz lineshape dip (the 4th line of the upper panel in Fig. 4). (ii) $0 < \Delta < \pi$ is left-low-right-high asymmetry Fano shape (the 3rd line of the upper panel in Fig. 4). (iii) $\Delta \sim \pi$ gives symmetry Lorentz lineshape peak (the 2nd line of the upper panel in

Fig. 4). (iv) $\pi < \Delta < 2\pi$ shows left-high-right-low asymmetry Fano shape (the 1st line of the upper panel in Fig. 4). The Δ varies with the frequency of the incident light, thus we observed all four different lineshape types in the transmission spectra. Then, interference line shapes are formed. But unlike the waveguide coupled case, the energy flow irradiates into all directions in free space. So the spectrum collected by a detector in a particular direction has no energy conservation relationship with MII, which makes the evaluation of pumping efficiency from transmission spectrum invalid. That is why we turn to choose the MII as pumping efficiency indicator. In addition, the phase also varies according to different position of the detector making different lineshapes [27].

V. DETAILS OF EXCITATION PROCESS

The resonant mode of deformed quadrupole microcavity has its favorite emission direction. Hence the free space coupling should be the most effective under a particular pumping condition, as a reversal of directional emission from deformed microcavity [27]. Here, we studied the pumping with different parameters (θ, x) [Fig. 2], and recorded the MIIs of four quadrupole microcavities ($\epsilon = 0.00, 0.05, 0.10, 0.15$) as illustrated in Fig. 5. MIIs of circular cavity ($\epsilon = 0$) do not change with the rotation angles because of the rotational symmetry of the cavity. Moreover, the maximum of MII occurs beyond the boundary, which indicates the most effective way of excitation the circular cavity is barrier tunneling. The slightly deformed quadrupole cavity with deformation of 0.05 has angle selectivity. Nevertheless, the main excitation manner is still tunneling, since the maximum pump position is outside the cavity too. In addition, MII distribution of this cavity shows a roughly horizontal symmetry, which is a result of the tunneling coupling showing CW and CCW symmetry. However, in quadrupole

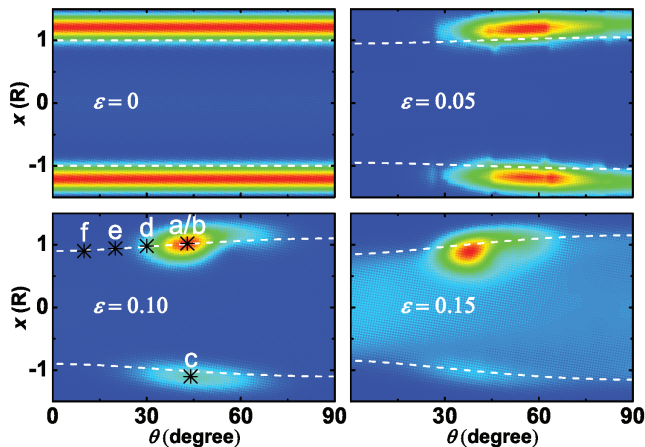


Figure 5. Pump efficiency distributions of quadrupole cavities with $\varepsilon = 0.00, 0.05, 0.10, 0.15$ in real space position coordinates (θ, x) . The frequency of incident beam fixed on resonance with the $q = 2$ mode. White dash lines are the projection boundary of cavity in x axis. Because of the discrete symmetry, it is sufficient only $0^\circ < \theta < 90^\circ$ is investigated.

cavity with deformation of 0.10, the highest MII area is located near the boundary projection line, i.e. incident beam is tangential to the boundary of the cavity. Because the width of the incident beam is not zero, half of the lights enter into the cavity by refraction. The size of the strong excitation region in the $\theta - x$ figure shrinks significantly comparing with the slightly deformed case. This localization suggests strengthening of selectivity of pumping angle. In addition, the MII of highest excitation region in the upper part of the figure is much stronger than that of the second highest excitation region lying in the lower part. Different from the barrier tunneling coupling where the tunneling rate only depends on the local curvature and is same for CW and CCW wave, the dynamical tunneling coupling is sensitive to the energy distribution of the incident beam in the chaotic sea of phase space. The dynamics of rays incident in these two regions are non-identical due to the asymmetric unstable manifold in the chaotic sea, thus the energy distributions in cavity for these two excitation conditions are different, and finally raises different excitation efficiency to high-Q modes by dynamical tunneling. By increasing the deformation to 0.15, the highest MII zone is mainly located inside the boundary projection line, which suggests refraction excitation. This is the only optimal position as the dynamical tunneling dominates the pumping process. And the MII is visible when a beam shines on the cavity which is due to low contrast to the optimal coupling. The MII is always nonzero when light shines on the cavity.

As the inverse process of emission, excitation of an ARC should show some correspondence with directional emission. For example, comparing our pumping efficiency with the emission figure obtained in Ref. [15], they show great consistence. In order to express this correlation directly, MII distribution ($\varepsilon = 0.1$ panel of Fig. 5)

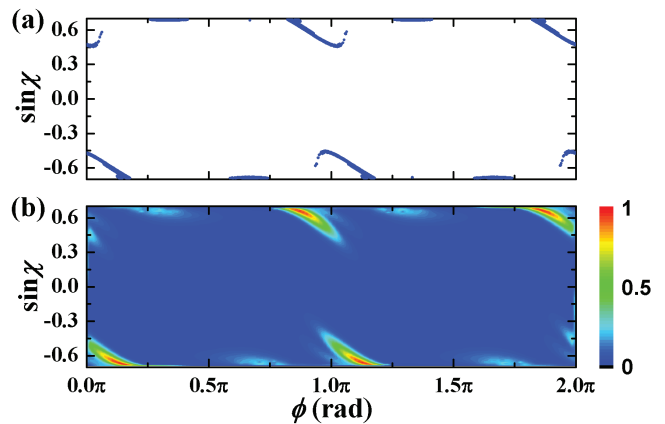


Figure 6. (a) Emissions of the quadrupole cavity with $\varepsilon = 0.1$ predicted with ray optics. The points in the figure are rays whose reflection angles are larger than the critical total reflection angle. So, collections of refractions of those rays constitute the emission picture. (b) Phase space presentation of $\varepsilon = 0.1$ panel of Fig. 5.

is projected to phase space [Fig. 6(b)] by ray trajectory. First, each point in real space distribution is treated as rays. The rays impacted on the cavity (points between the white dash line) can refract into the cavity. Then, record pairs of refracting positions and the sine of refraction angles $(\phi, \sin \chi)$ with pump efficiency denotative intensity. For comparison, the phase space presentation of emission property of the same cavity is obtained by ray simulation [Fig. 6(a)]. Those two distributions in phase space show good consistence. Thus, the excitation is verified numerically as inverse process of emission.

To investigate the detail of the excitation process and get a deep physical insight of the free space coupling, Husimi projections of the excitation (purple background picture in Fig. 7) are calculated for different pump condition. As demonstrated in Fig. 7(g), Husimi of the optimum excitation is consistent with the Husimi of order-2 mode [see Fig. 1(c) green dots] in CCW half phase plane. It shows that the incident energy is coupled into the cavity and forms resonant traveling mode [Fig. 7(a)]. The excitation process is also demonstrated in the case of detuning light ($kR = 50$) with the same geometry [Fig. 7(b)]. The Husimi projection of the detuning excitation has four dense points which have good superposition area with the resonance islands. Next, the excitation field corresponding to the second maximum MII configuration, i.e. the optimal excitation on the other side, is obtained [Fig. 7(c)]. It is a resonant order-2 CW mode as is shown in SOS [Fig. 1(c)]. The right side patterns in Fig. 7 are the distributions of excitation CCW mode by tangential incident beam at the rotating angle of 30° [Figs. 7(d), (j)], 20° [Figs. 7(e), (k)] and 10° [Figs. 7(f), (l)], respectively. The corresponding Husimi projections reflect the change of coupling strengthens between the incident beam and the resonance mode from strong to weak. The mode built in 30° case is merely strong, while the mode of

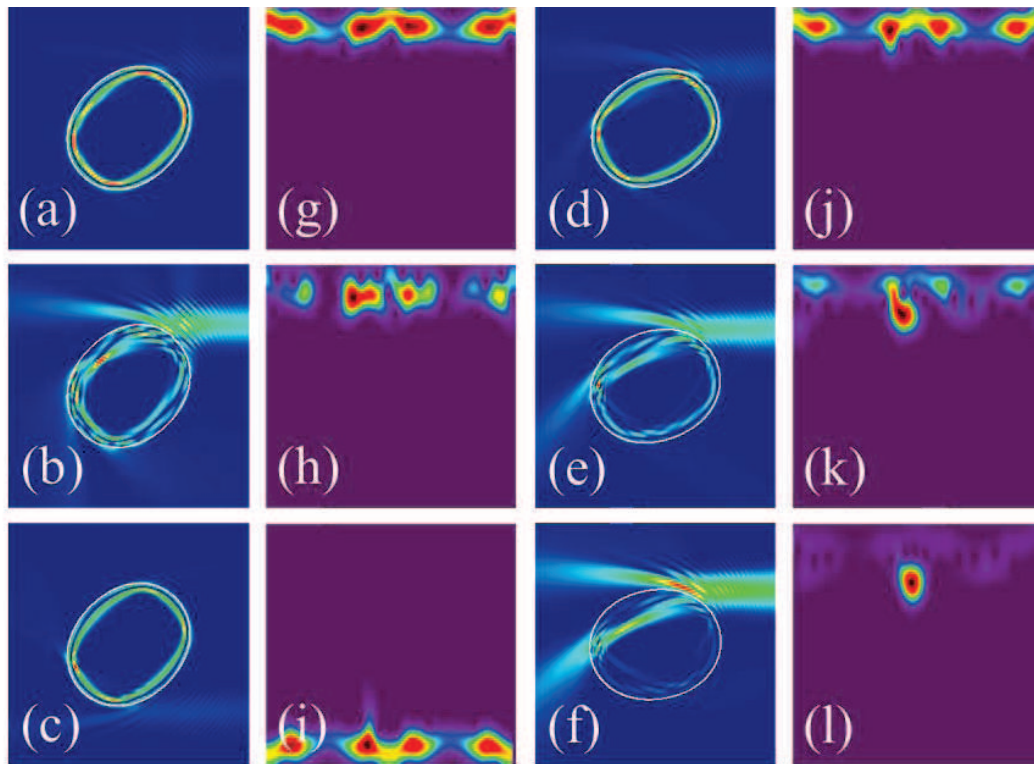


Figure 7. False color intensity patterns of excited cavity ((a), (b), (c), (d), (e), and (f)) and corresponding Husimi projection ((g), (h), (i), (j), (k), and (l)). The aim distances and the rotation angles are labeled with corresponding letters in $\varepsilon = 0.1$ panel of Fig. 5. The coordinates of real space patterns and phase space projection are the same with Fig 3(a) and Fig. 1(c), respectively.

20° only has four weak points in the SOS. As for the 10° , only very subtle mode energy emerges in the SOS. As we can see in the phase space, the more overlap between the incident beam and the resonant mode there is, the higher excitation MII will be established. The overlap owes to the wave character of the beam. Despite the penetration into islands is forbidden for the refraction rays from the outside, the dynamical tunneling effect allows it.

VI. CONCLUSION

We have gotten the inner and outer field of the excitation cavity by BEM. Scattering energy flow was also calculated with the Poynting vector. The transmission spectrum of a certain direction can have asymmetric line-shape because of the interference. MII distribution agrees well with the emission picture in reverse manner in phase

space. MII distributions of cavity with different deformations also exhibit two main excitation processes, i.e. barrier tunneling and dynamic tunneling. Besides the frequency matching, the sufficient overlap between the incident beam and the resonance mode is the key factor for efficient excitation.

ACKNOWLEDGMENTS

This work was supported by the National Natural Science Foundation of China under Grant No.11204196/11004184, the National Fundamental Research Program of China under Grant No. 2011CB921200, the Knowledge Innovation Project of Chinese Academy of Sciences, the Fundamental Research Funds for the Central Universities, and the Foundation of He'nan Educational Committee of China under Grant No. 2011A140021.

[1] K. J. Vahala, Nature (London) **424**, 839 (2003).

[2] S. Qian, J. Snow, H. Tzeng, and R. Chang, Science (New York) **231**, 486 (1986).

[3] A. B. Matsko, A. A. Savchenkov, D. Strekalov, V. S. Ilchenko, and L. Maleki, IPN Progress Report **42**, 162 (2005).

[4] S. Haroche and D. Kleppner, Phys. Today **42**, 24 (1989).

- [5] Y. Xiao, Y. Liu, B. Li, Y. Chen, Y. Li, and Q. Gong, *Phys. Rev. A* **85**, 031805 (2012).
- [6] F. Vollmer and S. Arnold, *Nature Methods* **5**, 591 (2008).
- [7] Y. Park and H. Wang, *Nature Phys.* **5**, 489 (2009).
- [8] J. Nöckel and A. Stone, *Nature* **385**, 45 (1997).
- [9] Gmachl *et al.*, *Science* **280**, 1556 (1998).
- [10] G. D. Chern *et al.*, *Appl. Phys. Lett.* **83**, 1710 (2003).
- [11] W. Fang, A. Yamilov, and H. Cao, *Phys. Rev. A* **72**, 023815 (2005).
- [12] J. Wiersig and M. Hentschel, *Phys. Rev. Lett.* **100**, 33901 (2008).
- [13] Y. Xiao *et al.*, *Opt. Lett.* **34**, 509 (2009).
- [14] C. L. Zou *et al.*, arXiv:0908.3531 (2009).
- [15] S.-Y. Lee and K. An, *Phys. Rev. A* **83**, 023827 (2011).
- [16] S.-B. Lee *et al.*, *Appl. Phys. Lett.* **90**, 041106 (2007).
- [17] J. Yang *et al.*, *Appl. Phys. Lett.* **93**, 061101 (2008).
- [18] J. Yang *et al.*, *Opt. Express* **18**, 26141 (2010).
- [19] R. Schäfer, U. Kuhl, and H. Stöckmann, *New J. Phys.* **8**, 46 (2006).
- [20] H. Schwefel *et al.*, *J. Opt. Soc. Am. B* **21**, 923 (2004).
- [21] J. Wiersig, *J. Opt. A* **5**, 53 (2003).
- [22] C.-L. Zou, H. G. L. Schwefel, F.-W. Sun, Z.-F. Han, and G.-C. Guo, *Opt. Express* **19**, 15669 (2011).
- [23] J. Unterhinninghofen, J. Wiersig, and M. Hentschel, *Phys. Rev. E* **78**, 016201 (2008).
- [24] D. Oron and Y. Silberberg, *J. Opt. Soc. Am. B* **21**, 1964 (2004).
- [25] M. Hentschel and M. Vojta, *Opt. Lett.* **26**, 1764 (2001).
- [26] C. Zou *et al.*, *J. Opt. Soc. Am. B* **26**, 2050 (2009).
- [27] C. Zou *et al.*, arXiv:1209.1442 (2012).